FULL PAPER

Lithium and Sodium Storage

ADVANCED
ENERGY
MATERIALS

www.advenergymat.d

Check for updates

Bottom-Up Confined Synthesis of Nanorod-in-Nanotube Structured Sb@N-C for Durable Lithium and Sodium Storage

Wen Luo, Feng Li, Jean-Jacques Gaumet,* Pierre Magri, Sébastien Diliberto, Liang Zhou, and Liqiang Mai*

Antimony (Sb) has emerged as an attractive anode material for both lithium and sodium ion batteries due to its high theoretical capacity of 660 mA h g^{-1}. In this work, a novel peapod-like N-doped carbon hollow nanotube encapsulated Sb nanorod composite, the so-called nanorod-in-nanotube structured Sb@N-C, via a bottom-up confinement approach is designed and fabricated. The N-doped-carbon coating and thermal-reduction process is monitored by in situ high-temperature X-ray diffraction characterization. Due to its advanced structural merits, such as sufficient N-doping, 1D conductive carbon coating, and substantial inner void space, the Sb@N-C demonstrates superior lithium/sodium storage performance. For lithium storage, the Sb@N-C exhibits a high reversible capacity (650.8 mA h g^{-1} at 0.2 A g^{-1}), excellent long-term cycling stability (a capacity decay of only 0.022% per cycle for 3000 cycles at 2 A g^{-1}), and ultrahigh rate capability (343.3 mA h g^{-1} at 20 A g^{-1}). For sodium storage, the Sb@N-C nanocomposite displays the best long-term cycle performance among the reported Sb-based anode materials (a capacity of 345.6 mA h g^{-1} after 3000 cycles at 2 A g^{-1}) and an impressive rate capability of up to 10 A g^{-1}. The results demonstrate that the Sb@N-C nanocomposite is a promising anode material for high-performance lithium/sodium storage.

W. Luo, F. Li, Prof. L. Zhou, Prof. L. Q. Mai
State Key Laboratory of Advanced Technology for Materials
Synthesis and Processing
International School of Materials Science and Engineering
Wuhan University of Technology
Luoshi Road 122, Wuhan 430070, P. R. China
E-mail: mlq518@whut.edu.cn
W. Luo, Prof. J.-J. Gaumet, Dr. P. Magri
Laboratoire de Chimie et Physique: Approche Multi-échelles
des Milieux Complexes (LCP-A2MC)
Institut Jean Barriol
Université de Lorraine
Metz 57070, France
E-mail: jean-jacques.gaumet@univ-lorraine.fr
Dr. S. Diliberto
Institut Jean Lamour
UMR CNRS 7198
Université de Lorraine
Campus Artem
2 allée André Guinier, Nancy 54000, France
Dr. L. Q. Mai
Department of Chemistry
University of California
Berkeley, CA 94720, USA

The ORCID identification number(s) for the author(s) of this article can be found under https://doi.org/10.1002/aenm.201703237.

1. Introduction

The deployment of renewable energy technologies critically depends on the low-cost and scalable energy storage systems. Lithium-ion batteries (LIBs), which have revolutionized and dominated the market of portable electronics, are emerging as one of the most encouraging choices as reliable energy storage device.[1–3] Nevertheless, the transition from portable electronics to electric vehicles (EVs) and smart grid still requires a substantial improvement in current-level energy and power density of LIBs. Therefore, pursuing novel electrode materials with high theoretical capacity becomes of great importance.[4] In the case of anode materials, alloy anode materials have triggered paramount research interests due to their high theoretical capacities and safe operation potential.[5–10] Among them, antimony (Sb) is regarded as a promising candidate because of its high theoretical capacity of 660 mA h g^{-1}, low polarization (≈0.2 V), and suitable working voltage (0.8–0.9 V vs Li$^+$/Li).[5] Additionally, Sb is also an attractive anode material for sodium-ion batteries (SIBs), which are brought as a substitute or even a replacement to LIBs concerning the limited lithium resource.[11] In spite of the above-mentioned merits, the relative low conductivity and large volume expansion of Sb eventually result in the particle pulverization and loss of electrical contact along with rapid capacity decay, which severely restrict its practical long-term application.[12–16]

In recent years, much efforts have been made to address the inferior electrochemical performance issues by designing novel architectures (such as nanowire arrays[17] or hollow structure[18–20]) or introducing carbonaceous materials to enhance the conductivity.[21–38] For instance, Liu et al. recently synthesized hollow Sb@C yolk–shell spheres as anode materials by a new nanoconfined galvanic replacement method, showing much improved electrochemical performance in both LIBs and SIBs.[20] Wang et al. demonstrated that the oxygen-deficient TiO$_2$ could work as a perfect interface material for high-performance Sb anode, and the achieved double-wall crystalline Sb@amorphous TiO$_{2-x}$ nanotubes displayed a reversible capacity of 300 mA h g^{-1} after 1000 cycles at 2.64 A g^{-1} in SIBs.[29] Another worth-mentioning work accomplished by Lou and co-workers is to design and construct Sb@C coaxial nanotubes,

ADVANCED
SCIENCE NEWS
www.advancedsciencenews.com

ADVANCED
ENERGY
MATERIALS
www.advenergymat.de

which manifest the best rate performance among the reported Sb-based anode materials for SIBs.[28] Nevertheless their electrochemical performances, especially the long-term cycling stability, are still far from satisfactory. Recently, suitable N-doped carbon layer coating has shed light on high-performance electrode materials because it can not only increase the electronic conductivity but also create numerous extrinsic defects and active sites for ion diffusion facilitating when the ions insert/extract in the carbon layer.[39–41] In fact, however, most of previous works involve multistep top-down methods of evaporation or infiltration and delicate instruments to confine active materials into/on carbon nanotube or N-doping carbon sheet.[25,26,34] Bottom-up confined synthesis can allow the delicate control of materials at nanoscale.[42] For instances, Cui and co-workers developed a one-step bottom-up approach to construct hollow nanostructured sulfur for high-performance Li–S batteries.[43] In our work, a conductive polymer, polypyrrole (PPy), which originally consists of abundant pyrrolic N in its chain structure, is selected as an ideal contributor to construct N-doped carbon hollow nanotube encapsulated Sb nanorod architecture, the so-called nanorod-in-nanotube structure, through a facile one-step bottom-up approach.
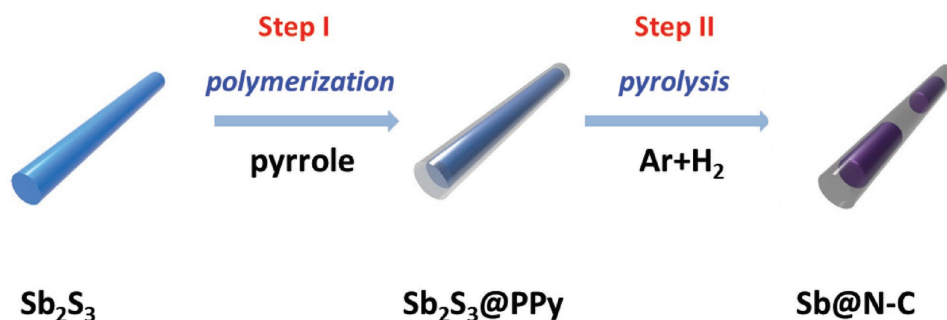
Herein, an N-doped carbon hollow nanotube encapsulated Sb nanorod composite (denoted as Sb@N-C) is fabricated by the in situ carbonization and reduction of Sb_2S_3@PPy nanorods produced by the polymerization of pyrrole monomer on Sb_2S_3 nanorods. The formation of Sb nanorods and left void space within carbon nanotubes could be assigned to the facile in situ reduction of Sb_2S_3 into crystalline Sb. Meanwhile, the PPy coating layer is transformed into amorphous N-doped carbon hollow nanotubes. Thus, the sufficient void space can perfectly accommodate the volumetric expansion during the Li/Na-ion insertion, and thus endowing robust structural stability to the material. More importantly, the uniform N-doped carbon coating layer can improve the overall electronic conductivity and facilitate the Li^+/Na^+ diffusion. Accordingly, such a unique structure is endowed with excellent electrochemical performances as anode materials for both LIBs and SIBs.
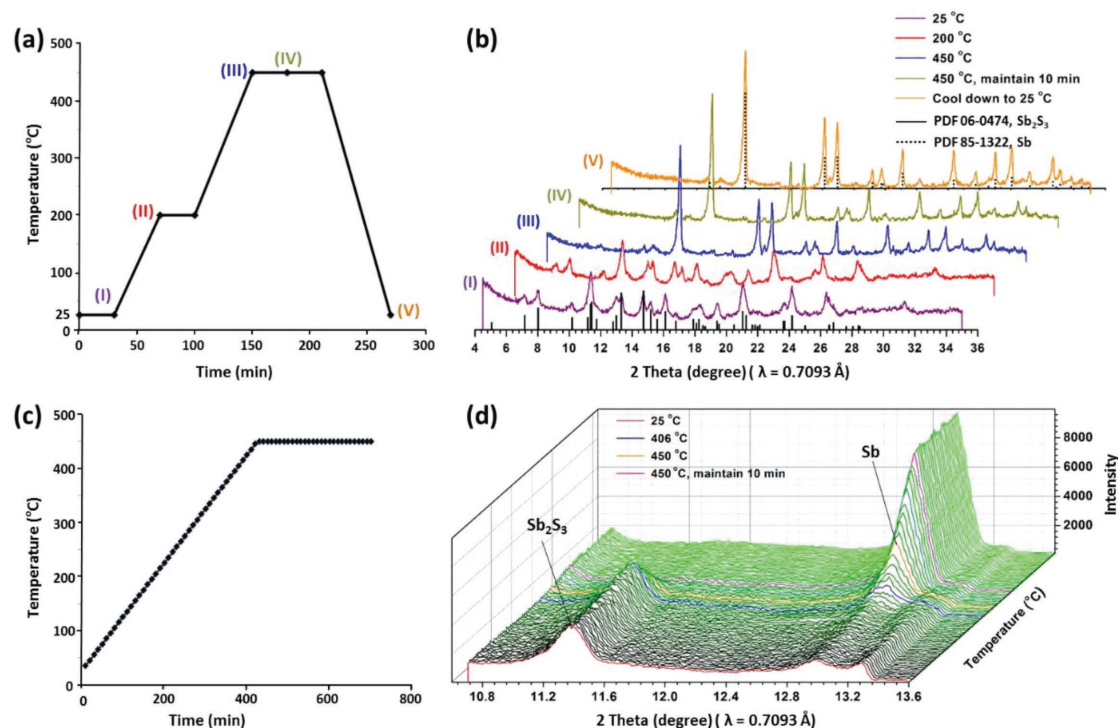
2. Results and Discussions

The schematic illustration of the construction of Sb@N-C is provided in **Figure 1**. First, high-quality rhombohedral phase Sb_2S_3 nanorods (Figure S1, Supporting Information) were synthesized through a facile hydrothermal process. The achieved Sb_2S_3 nanorods exhibit a narrow size distribution with an average diameter of 90 nm and lengths up to hundreds of micrometers. Based on a well-developed room-temperature polymerization process, the Sb_2S_3 nanorods functioned as the template and were successfully coated by a uniform layer of PPy (step I, Figure 1). The X-ray diffraction (XRD) pattern of Sb_2S_3@PPy (Figure S2a, Supporting Information) reveals that Sb_2S_3 is still the only crystalline phase without any other impurities after the introduction of polymer coating. After the polymerization of pyrrole, the nanorods can well maintain the 1D structure to form Sb_2S_3@PPy core–shell nanorods with a uniform thickness of 15 nm PPy coating layer (Figure S2b–f, Supporting Information). The corresponding elemental mapping images of Sb_2S_3@PPy confirm the uniform distribution of Sb, S, C, and N (originated from PPy) within the structure (Figure S2g–k, Supporting Information). The presence of PPy coating layer in the Sb_2S_3@PPy composite was further confirmed by Fourier transform infrared spectroscopy spectra (Figure S3, Supporting Information). The subsequent calcination treatment of the Sb_2S_3@PPy core–shell nanorods in H_2/Ar atmosphere contributed to the formation of Sb@N-C hybrid structure (step II, Figure 1).

In order to investigate the in situ formation of crystallographic phases during annealing, high-temperature XRD (HT-XRD) was used as a powerful technique to provide insightful information.[44,45] **Figure 2**a shows a multistep annealing protocol to study phase transformation. This protocol includes two-step heating, followed by a maintaining stage at 450 °C, then cooling down to room temperature. The initial XRD pattern (line I, Figure 2b) displays typical diffraction peaks consistent with structure of pure rhombohedral phase Sb_2S_3 (powder diffraction files (PDF) No. 06-0474), and no distinctive phase evolution is detected when the temperature reaches 200 °C (line II, Figure 2b). The sharp XRD peaks for Sb (PDF No. 85-1322) appear when the temperature arrives at 450 °C (line III, line IV, Figure 2b), implying that a significant phase transformation has involved once a temperature of 450 °C is attained. Furthermore, it is found that the reduced product Sb with high crystalline degree can exist stably when cooling down to room temperature again (line V, Figure 2b). In order to obtain more vivid and time-resolved insight into the in situ formation of Sb nanocomposite, we present a series of high-resolution in situ XRD scans recorded every minute in a narrow 2θ range of 10.8°–13.6°. The target temperature is set as 450 °C, as indicated by the above interval HT-XRD results. And the corresponding operando temperature-time profiles are shown in Figure 2c. These real-time

Figure 1. Schematic illustration of the construction of peapod-like Sb@N-C hybrid.
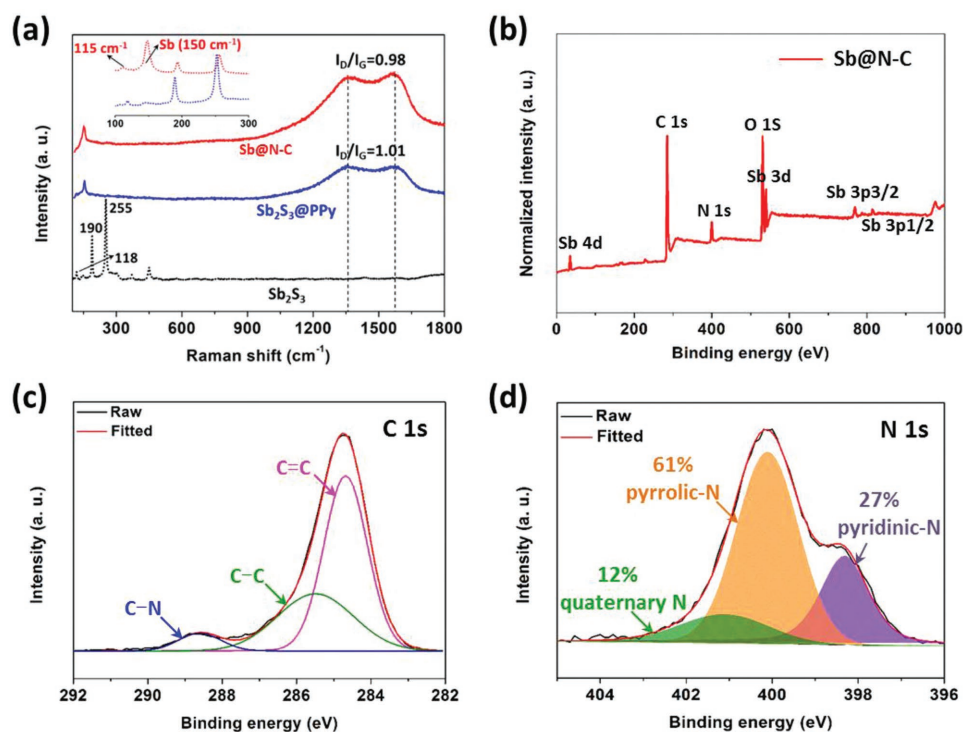
**ADVANCED
SCIENCE NEWS**
www.advancedsciencenews.com

**ADVANCED
ENERGY
MATERIALS**
www.advenergymat.de

Figure 2. a) Temperature–time profiles of a multistep heating program used to anneal $Sb_2S_3@PPy$ precursor materials. Note that every black circle indicates individual XRD measurements. b) Five typical XRD patterns recorded from marked individual measurement of Figure 2a. c) Temperature–time profiles with a constant heating rate from room temperature to 450 °C. d) Series of in situ HT-XRD profiles recorded during the complete annealing process corresponding to Figure 2c.

scans demonstrate, to a large extent, the fast and complete transformation from Sb_2S_3 to Sb, as displayed in Figure 2d. In details, the intensity of (310) reflections at 11.4° for rhombohedral phase Sb_2S_3 gradually decrease, which indicated the continually reduction of Sb_2S_3 during annealing. Simultaneously, the (012) diffraction of Sb at $2\theta = 13.3°$ emerge when the temperature reaches 406 °C (yellow profile). Notably, the transformation of Sb_2S_3 to metallic Sb is principally completed when the temperature arrives at 450 °C and further maintained for 10 min (pink profile). Thus the above results manifest that the reduction of Sb_2S_3 to Sb during annealing is a quite rapid and facile process.

Interestingly, we disclose that the carbon layer in situ derived from PPy polymer coating can not only release thermal stress but also positively accelerate the reduction process under H_2/Ar atmosphere. Ex situ scanning electron microscopy (SEM) measurements show that bare Sb_2S_3 nanorods distort or aggregate during annealing (Figure S4a1–a4, Supporting Information). As a comparison, the $Sb_2S_3@PPy$ nanorods can retain the 1D structure and ensure the formation of complex peapod-like nanorod-in-nanotube structure (Figure S4b1–b4, Supporting Information). Ex situ XRD analysis reveals that annealing the bare Sb_2S_3 nanorods at 450 °C even for 75 min does not lead to diffraction peaks for Sb (Figure S5a, Supporting Information). In contrast, pure phase Sb can be achieved by annealing $Sb_2S_3@PPy$ at 450 °C for a favorable duration of 45 min (Figure S5b, Supporting Information). We assume that the mass of sample and heat transfer effect are responsible for the different duration for reduction with respect to HT-XRD and ex situ XRD test.[38]

Raman measurement was conducted to study the local structure and carbon characteristic. It should be noted here the measurements were operated at a wavelength of 532 nm (solid lines in **Figure 3**a) or 633 nm (dot lines in Figure 3a) as the excitation source in order to collect distinctive different Raman modes of metallic composites and carboneous materials. The pristine Sb_2S_3 exhibits three resonant peaks at about 118, 190, and 255 cm^{-1}, which are in agreement with the typical frequencies of Sb_2S_3.[46] The Raman spectra of $Sb_2S_3@PPy$ and Sb@N-C show smooth D- and G-bands for carbon at 1365 and 1580 cm^{-1}, corresponding to disordered and graphitic structure of carbon, respectively. The I_D to I_G ratio of Sb@N-C (≈0.98) is lower that of $Sb_2S_3@PPy$ (≈1.01), which suggests the degree of graphitization was mildly increased after pyrolysis. Additionally, the vibrations centered at 115 and 150 cm^{-1} which are correlated to Sb confirm the success formation of Sb in the product.[47]

X-ray photoelectron spectroscopy (XPS) spectrum of Sb@N-C is provided in Figure 3b. The signals of Sb, C, and N can be easily observed in the survey spectrum. To make a careful analysis on N-doping state, high-resolution XPS spectra were collected. In the C1s spectrum of Sb@N-C (Figure 3c), the peaks centered at 284.6 and 285.5 eV can be attributed to C=C and C—C bonding configurations, respectively.[39] Notably, a small peak located at a higher value of 288.6 eV, which can be ascribed to C—N, indicates the doping of N into carbon layer.[48] Meanwhile, N-doping types and corresponding contents of Sb@N-C were analyzed, as depicted in the XPS results of N1s

ADVANCED
SCIENCE NEWS
www.advancedsciencenews.com

ADVANCED
ENERGY
MATERIALS
www.advenergymat.de

Figure 3. Raman spectra of Sb_2S_3, Sb_2S_3@PPy, and Sb@N-C a), XPS survey spectrum of Sb@N-C b), high-resolution C 1s c), and N 1s d), XPS spectra of Sb@N-C.

(Figure 3d). The spectrum is deconvoluted into three contributions, namely pyridinic N (398.5 eV), pyrrolic N (400.1 eV), and quaternary N (401.1 eV).[39] It can be clearly seen that pyrrolic N is dominant (61% in ratio) compared to the other two N types, which benefits from the intrinsic pyrrolic N defects in the macromolecular of PPy coating. It can be anticipated that sufficient pyridinic N and pyrrolic N doping would induce numerous extrinsic defects and active sites for rapid ion diffusion and thus enhance the electrochemical performance.[39,48,49]

The typical SEM images of Sb@N-C are provided in **Figure 4**a,b. After annealing, the 1D nanostructure maintains well without collapse, and the created void space can be easily observed by the contrast. The sample displays a nanorod-in-nanotube morphology with a length of several micrometers and an average diameter of about 110 nm. Besides, these well-defined nanorods possess a smooth surface, implying polymerization process has successfully contributed to a uniform coating layer. Transmission electron microscope (TEM) image (Figure 4c) of the Sb@N-C confirms that as-synthesized sample is characterized with a unique peapod-like nanorod-in-nanotube morphology. Segment-like Sb nanorods are well confined within a ≈11 nm thick carbon layer, as shown in the inset of Figure 4c. The thickness of carbon coating is mildly decreased compared to the original PPy layer (15 nm) due to the shrinkage of polymer during annealing. The nanorod-in-nanotube morphology design would be a tradeoff to maximum volumetric energy density without sacrificing the cyclability compared to solid core–shell structure or simple hollow nanotube. Energy-dispersive X-ray measurement (Figure S6, Supporting Information) demonstrates that Sb and C peaks are remarkably observed without any signal of S, confirming the complete transformation from

Sb_2S_3@PPy into Sb@N-C. High-resolution TEM (HRTEM) image (Figure 4d) of Sb@N-C presents clear lattice fringes with spacing of about 0.215 nm, which can be assigned to the (110) planes of Sb. The selected area electron diffraction (SAED) pattern (Figure 4e) indicate the single crystal structure, and the bright diffraction spots can be indexed with standard rhombohedral phase Sb. Additionally, elemental mappings (Figure 4f–j) reveal that C and N are uniformly distributed throughout the carbon nanotube; in contrast, Sb is confined to partially occupy the inner space of the tube, clearly revealing the peapod-like nanorod-in-nanotube structure. The Sb content in the Sb@N-C was measured by thermogravimetric analysis (TGA) (Figure S7, Supporting Information), based on the mass loss of carbon combustion and the weight gain of Sb_2O_4 formation, the total Sb content in the composite was calculated to be 60.8 wt%. Brunauer-Emmett-Teller (BET) surface of Sb@N-C is measured to be 14.8 m^2 g^{-1} (Figure S8, Supporting Information).

To evaluate the lithium storage performance of Sb@N-C, 2016-type coin cells were assembled using metallic Li foil as the counter electrode. Note that the specific capacity in this work is calculated based on the total mass of the Sb@N-C hybrid. **Figure 5**a shows cyclic voltammograms (CV) of Sb@N-C during the first three cycles for LIBs. During the first cathodic scan, a sharp peak located at 0.79 V attributed to the lithiation reaction from metallic Sb to Li_3Sb and a peak near 0.01 V caused by the lithium ion insertion into carbonaceous materials can be observed;[50] the anodic peak centered at 1.08 V could be ascribed to the dealloying process from Li_3Sb to Sb.[19] In the subsequent scans, the curves nearly overlap with the first one, confirming the high reversibility and stability of Sb@N-C. Figure 5b presents the typical lithiation–delithiation voltage profiles
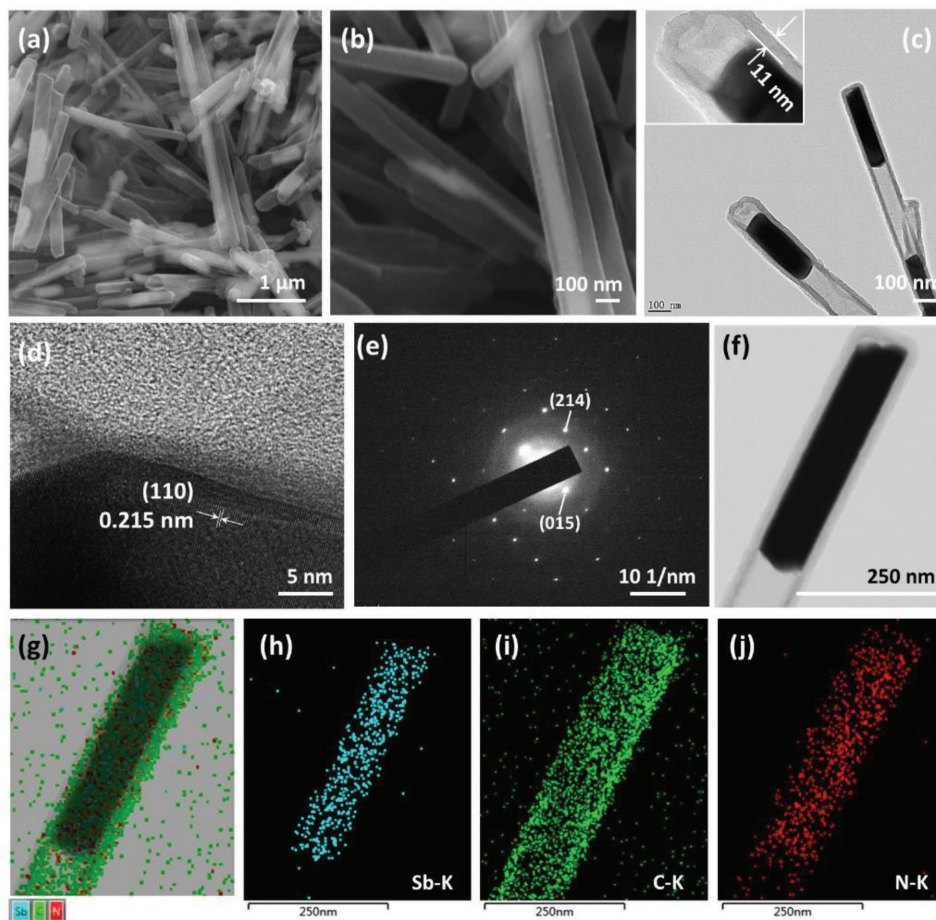
Figure 4. SEM images a,b), TEM image c), HRTEM image d), SAED pattern e), TEM image f), and energy-filtered transmission electron microscopy (EFTEM) element mapping images g–j) of Sb@N-C.

of Sb@N-C for the first three cycles at a current density of 200 mA g^{-1}. The electrode delivers discharge and charge capacities of 831.5 and 650.8 mA h g^{-1}, respectively, which corresponds to an initial Coulombic efficiency (CE) of 78.3%. Furthermore, the discharge profiles of first three cycles are characterized by an obvious plateau around 0.79 V, which are well consistent with the above CV results. Figure 5c displays the cycling performance of Sb@N-C at a current density of 200 mA g^{-1}. After 300 cycles, the reversible capacity can still retain at 602.8 mA h g^{-1} with a capacity retention of 92.7% (against 2nd discharge capacity), which reveals a highly stable cycling process. Expect for the first a few cycles, the subsequent CE stabilizes at around 100%. SEM characterization and elemental mapping (Figure S9, Supporting Information) reveal that the 1D nanorods morphology can be well maintained even after 300 cycles, confirming the robustness of PPy-derived carbon nanotube structure.

The rate performance of Sb@N-C anode in LIBs is then evaluated by charging/discharging at various current densities, as shown in Figure 5d and Figure S10 in the Supporting Information. The average reversible capacities of Sb@N-C are 641.2, 567.1, 509.4, 467.6, 426.6, and 379.9 mA h g^{-1} at current densities of 0.2, 0.5, 1, 2, 5, and 10 A g^{-1}, respectively. Notably, even a capacity of 343.3 mA h g^{-1} can be still maintained when a high

current density of 20 A g^{-1} is applied. Additionally, the discharge capacity of Sb@N-C can be recovered to 636.1 mA h g^{-1} and keep stably for the extended cycling when the current density returns to 0.2 A g^{-1}. These results indicate the excellent rate capability and cycling stability. Figure 5e further displays the long-term cyclability of Sb@N-C at a relative high current density of 2 A g^{-1}. Impressively, the Sb@N-C exhibits remarkable ultralong cycling stability. After 3000 cycles, the Sb@N-C can still deliver a capacity of 395 mA h g^{-1}. It demonstrates a slow capacity decay of only 0.022% per cycle. The lithium storage properties of Sb@N-C are among the best for Sb-based electrode materials (Figures S11 and S12, Supporting Information), especially in terms of specific capacity and long-term cyclability.[13,16,18–22,29–32] Electrochemical impedance spectroscopy (EIS) measurement of Sb@N-C electrode in LIBs was employed respectively before cycling. As can be seen in Figure S13 in the Supporting Information, the EIS plot of Sb@N-C anode was composed with an inclined line at low frequency and a depressed semicircle in the high frequency region. After simulation, the charge transfer resistance (R_{ct}) values for Sb@N-C are calculated to be 12.8 Ω, confirming its good electrical conductivity.

Since Sb has been demonstrated to be a promising alloying-based candidate for SIBs, the sodium storage performances of Sb@N-C were also examined in half cells. First, the CV
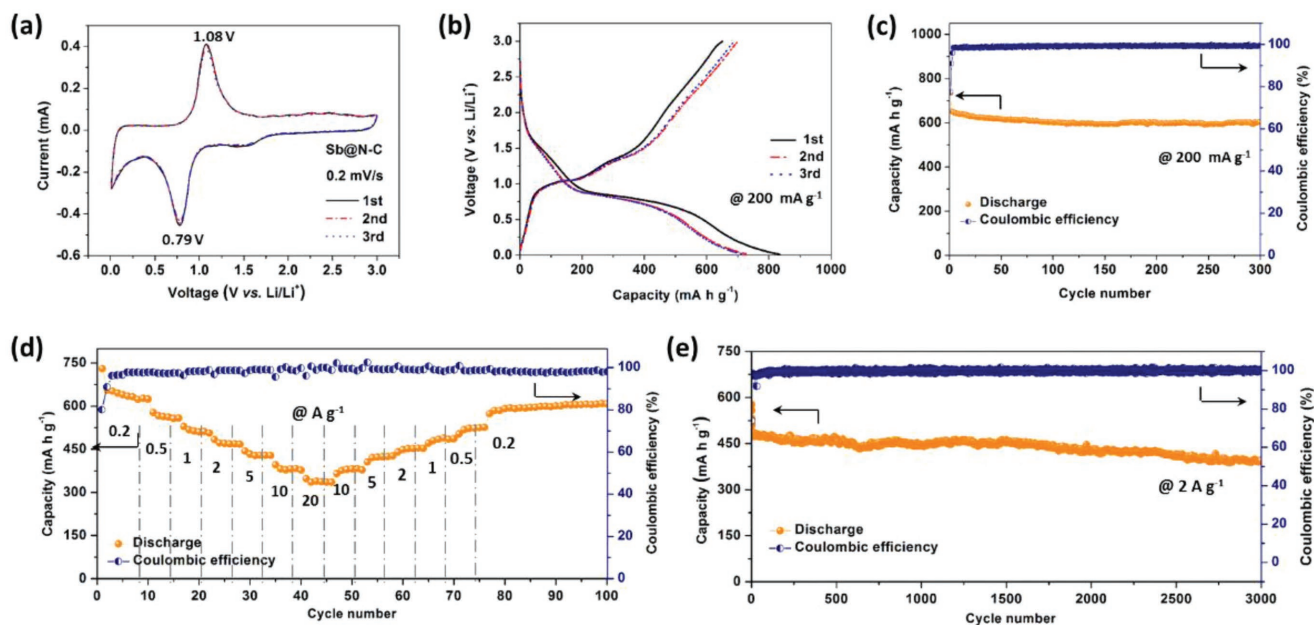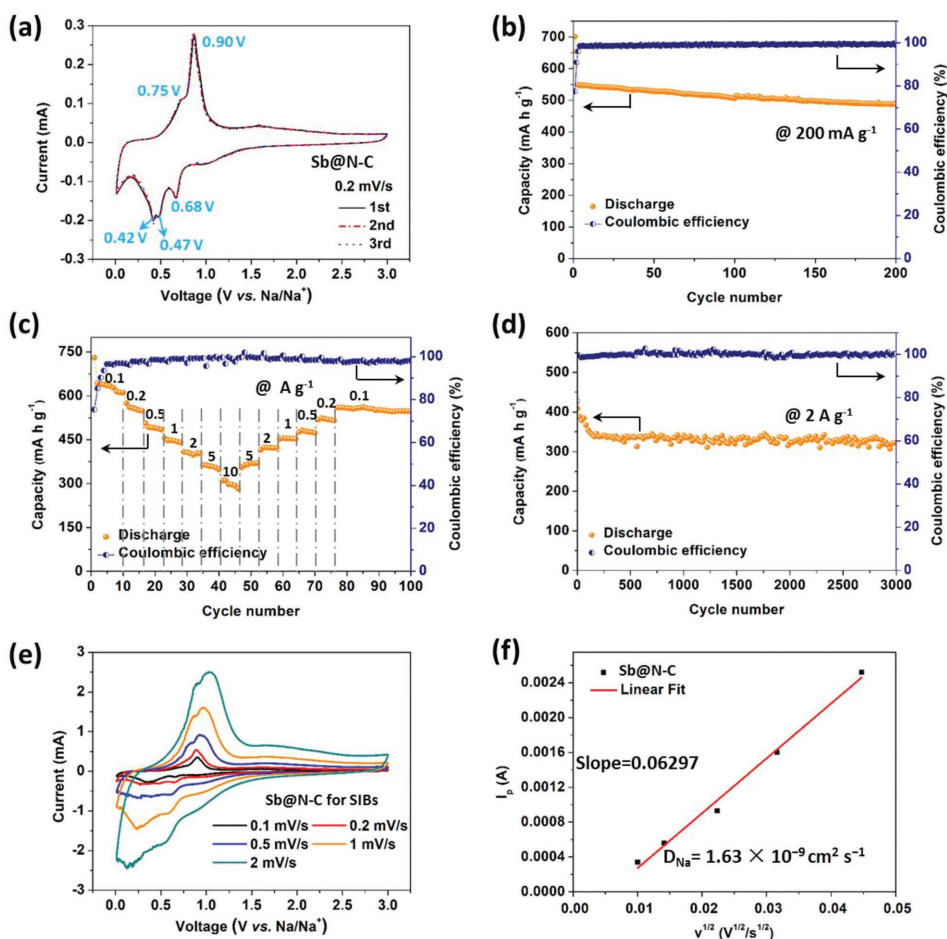
Figure 5. Electrochemical performances of Sb@N-C as an anode in LIBs: a) Cyclic voltammogram curves of Sb@N-C at a scan rate of 0.2 mV s^{-1}, b) first three charge–discharge profiles of Sb@N-C at a current density of 200 mA g^{-1}, c) cycling performance of Sb@N-C at a current density of 200 mA g^{-1}, d) rate performances of Sb@N-C at various current densities, e) long-term cycling performance of Sb@N-C at a current density of 2 A g^{-1}.

curves of Sb@N-C for the first three cycles at a scan rate of 0.2 mV s^{-1} between 0.01 and 3 V are illustrated in **Figure 6**a. During the first cathodic scan, the alloying reactions occur at about 0.68, 0.47, and 0.42 V, respectively. These reduction peaks can be ascribed to multistep Na–Sb alloying reactions.[16] The following anodic sweep is characterized by a shoulder peak centered at 0.75 V and a sharp peak around 0.9 V, which correspond to the desodiation of Na$_3$Sb and NaSb, respectively.[25] A pair of redox peaks near 0.01 V are attributed to the insertion/extraction of Na ions in the carbon layer.[22] The little different between the initial and subsequent scans is due to the formation of solid electrolyte interphase (SEI) layer. The CV profiles remain steady during first three scans, indicating that the Sb@N-C has good stability and reversibility for Na-ion insertion/extraction. At a current density of 200 mA g^{-1} the Sb@N-C displays a stable cycling process, as demonstrated in Figure 6b. The corresponding typical charge–discharge profiles of Sb@N-C anode in SIBs for the first three cycles are shown in Figure S14 in the Supporting Information. The Sb@N-C can deliver an initial capacity of 701.2 mA h g^{-1}; after 200 cycles, its capacity can still reach 487.6 mA h g^{-1}. Though the initial CE of Sb@N-C is 77.5%, it increases rapidly to 96% at the 3rd cycle and then remains steady at around 99% for the following cycles, revealing an outstanding reversibility for sodium storage.

Significantly, the Sb@N-C exhibits superior rate performance, as illustrated in Figure 6c and Figure S15 in the Supporting Information. The Sb@N-C delivers an average reversible capacity of 638.2 mA h g^{-1} at a current density of 0.1 A g^{-1}. When the current density increases to 10 A g^{-1}, the corresponding capacity retains as high as 309.8 mA h g^{-1}, exhibiting excellent rate capability. More importantly, the capacity could recover to 561.9 mA h g^{-1} when the current density returns to 0.1 A g^{-1}. It should be noted that the rate capability of Sb@N-C

in SIBs is inferior to that in LIBs (343.3 mA h g^{-1} can be still maintained at 20 A g^{-1}), which indicate the larger diameter of Na$^+$ ions results in more sluggish transportation and larger volume expansion. Figure S12 in the Supporting Information compares rate performance with those of previous reports on Sb-based anodes. The Sb@N-C hybrid exhibits much better rate capability than those of most reported SIBs anode materials.[19–29,32] Inspired by the good rate performance, a prolonged galvanostatic charge–discharge test of Sb@N-C was performed at a current density of 2 A g^{-1}, as presented in Figure 6d. In the first 200 cycles, the electrode experience a capacity decay which may be ascribed to following reasons: the decomposition of the electrolyte, the formation and stabilization of SEI film, and side effects caused by the irreversible reaction between Na$^+$ ions and the residual functional groups from PPy-derived carbon, which were also observed in other Sb/polymer-induced-carbon electrodes.[51] Afterward a high reversible capacity of up to 345.6 mA h g^{-1} can be still maintained after 3000 cycles, which suggests the superb cycling stability during ultrafast sodiation/desodiation process. SEM image (Figure S17, Supporting Information) of Sb@N-C after 3000 cycles show that though these nanorods slightly become shorter during long-term sodiation/desodiation process, they can still maintain the 1D structure and accommodate volumetric expansion. Ex situ TEM measurements were performed on Sb@N-C anode to study the structural evolution during a typical sodiation/desodiation process. It is clearly observed that the morphology of carbon nanotube did not change considerably (Figure S18a, Supporting Information) and the alloyed Sb nanorods encapsulated by carbon nanotube still maintain well. The measured lattice space of 0.42 nm (Figure S18b, Supporting Information) and the d-spacings of the rings in the SAED pattern of the sodiated sample (Figure S18c, Supporting Information) can be well indexed to

Figure 6. Electrochemical performances of Sb@N-C as an anode in SIBs: a) Cyclic voltammogram curves of Sb@N-C at a scan rate of 0.2 mV s^{-1}, b) cycling performance of Sb@N-C at a current density of 200 mA g^{-1}, c) rate performances of Sb@N-C at various current densities, d) long-term cycling performance of Sb@N-C at a current density of 2 A g^{-1}, e) CV curves at different sweep rates, and f) the corresponding relationship between peak currents and sweep rates.

a hexagonal Na$_3$Sb (PDF No. 74-1162), which provides strong evidence for the formation of Na$_3$Sb. Additionally, the single crystal structure of Sb can be detected at desodiated state after one cycle (Figure S18e,f, Supporting Information) and even 100 cycles (Figure S18h,i, Supporting Information), revealing the highly reversibility of Sb@N-C anode. The ultralong cyclability (3000 cycles) and high capacity retention (345.6 mA h g^{-1}) of the Sb@N-C are the best of reported anodes for SIBs (Figure S19, Supporting Information).[12,20–25,27–31,33,34,36–38]

To investigate the diffusion process of Na$^+$ ion and electrons in Sb@N-C, CV curves were measured with a series of scan rates from 0.1 to 2 mV s^{-1} (Figure 6e). The apparent diffusion coefficients for semi-infinite diffusion of Na$^+$ ion can be calculated based on the following Randles–Sevick equation

$$I_p = 2.69 \times 10^5 ACD^{1/2} n^{3/2} v^{1/2} \qquad (1)$$

where A stands for the anode area, C is the concentration of sodium ions in the anode, n is for the number of electrons transferred per molecule during the electrochemical reaction, v is for the scan rate (V s^{-1}), and D is the apparent Na$^+$ diffusion

coefficient of the whole electrode.[52] Plotting I_p as a function of $v^{1/2}$ gives rise to a straight line with a slope of about 0.06297 (Figure 6f). The apparent Na-ion diffusion coefficient D of the Sb@N-C anode is determined to be 1.63×10^{-9} cm^2 s^{-1}. The calculation validate that the N-doped carbon nanotube encapsulation could not only increase the electron conductivity but also effectively improve the Na$^+$ diffusion and thus boost its electrochemical performance. Furthermore, from the EIS plot of Sb@N-C anode in SIBs (Figure S20, Supporting Information), the charge transfer resistance (R_{ct}) was simulated and determined with a value of 21.9 Ω, which demonstrate the good charge transfer of achieved hybrid anode material.

The above results demonstrate the bottom-up confined construction of carbon nanotube encapsulated Sb nanorods lead to Sb@N-C anode with excellent lithium and sodium storage behaviors including remarkably high-rate performances and ultralong cyclability. The outstanding performance can be attributed to superior structural and chemical characteristics benefited from the novel design. Structurally, first, compared to bulk materials, the confined 1D Sb nanorods possess a great deal of active sites for lithium or sodium storage, contributing

**ADVANCED
SCIENCE NEWS**
www.advancedsciencenews.com

**ADVANCED
ENERGY
MATERIALS**
www.advenergymat.de

the high reversible capacity and rate capability. Second, the in situ formed carbon coating functions as an excellent buffer which reinforces the structural integrity, thus leading to its superior long-term cycling stability. Third, notably, this bottom-up thermal-reduction approach creates suitable inner void spaces which not only accommodate the volume expansion but also promote the ionic transport along the radial direction compared to solid nanorods. Chemically, sufficient N doping into carbon layer, especially pyridinic N and pyrrolic N, can significantly increase extrinsic defects and facilitate the diffusion and transport of electrons and ions.

3. Conclusion

In summary, we have fabricated a peapod-like carbon hollow nanotube encapsulated Sb nanorod hybrid by a facile bottom-up confinement thermal-reduction strategy. The resultant Sb@N-C hybrid is endowed with a robust highly conductive N-doping carbon coating layer, well-confined single-crystalline Sb nanorods, and a unique nanorod-in-nanotube architecture. Due to its composition and structure, the Sb@N-C nanocomposites exhibit superior lithium and sodium storage performances. Specifically, the Sb@N-C hybrid manifests an ultrahigh rate capability to deliver a lithium storage capacity of 343.3 mA h g^{-1} at 20 A g^{-1} and an impressive lifespan with a capacity of 395 mA h g^{-1} even after 3000 cycles at 2 A g^{-1}. As for Na-ion storage, the peapod-like Sb@N-C nanocomposites display the best long-term cycle performance among the reported Sb-based anode materials (up to 3000 cycles with a remarkable retained capacity of 345.6 mA h g^{-1}) and high rate capability up to 10 A g^{-1}. The outstanding electrochemical performances indicate the promising potential of Sb@N-C for next-generation energy storage. Moreover, this facile synthetic approach which takes the advantages of nanostructure design and doping defect regulation can be extended to the fabrication other advanced materials for energy related applications.

4. Experimental Section

All the reagents used in the experiment were of analytical grade and used without further purification.

Preparation of Sb$_2$S$_3$ Nanorods: The Sb$_2$S$_3$ nanorods were synthesized through a simple hydrothermal method based on a previous report.[24] Briefly, 4 mmol SbCl$_3$, 8 mmol C$_3$H$_7$NO$_2$S (L-cysteine), and 8 mmol Na$_2$S·9H$_2$O were orderly dissolved in 80 mL deionized water with constant stirring for 3 h. Then the above suspension was transferred into 100 mL Teflon-lined autoclave and kept at 180 °C for 12 h. After cooling down to room temperature, the product, Sb$_2$S$_3$ nanorods, was separated by centrifugation and washed with deionized water and ethanol for three times, afterward dried under vacuum at 70 °C overnight.

Preparation of Sb$_2$S$_3$@PPy Core–Shell Nanorods: To obtain the polypyrrole coated Sb$_2$S$_3$ core–shell nanorods (Sb$_2$S$_3$@PPy), 80 mg as-synthesized Sb$_2$S$_3$ nanorods and 4 mg sodium dodecyl sulfate were first dispersed into 40 mL deionized water with sonication for 0.5 h and the suspension was under stirring for 1 h. Afterward 21 µL pyrrole monomer was added and the mixture was further stirred for 1 h. Then the aqueous solution of oxidant, 4 mL (NH$_4$)$_2$S$_2$O$_8$ (0.1 M), was introduced into above suspension dropwise. The mixture solution was stirred at room temperature for 4 h and then centrifuged to isolate the black precipitate. The resultant product was washed with deionized water and ethanol for three times and dried through a freeze-drying process overnight.

Preparation of Peapod-Like Sb@N-C: To obtain Sb@N-C, the core–shell Sb$_2$S$_3$@PPy nanorods were calcined at 450 °C for 45 min under H$_2$/Ar (5:95, volume ratio) with a heating rate of 5 °C min^{-1}. To investigate the phase transformation and morphology evolution of Sb$_2$S$_3$ nanorods and Sb$_2$S$_3$@PPy nanorods, bare Sb$_2$S$_3$ nanorods and Sb$_2$S$_3$@PPy nanorods were calcined at 450 °C for 5, 15, 30, 45, 60, and 75 min, respectively, under H$_2$/Ar (5:95) with a heating rate of 5 °C min^{-1}.

Materials Characterization: XRD was employed to characterize the crystallographic information using a Bruker D8 Advance X-ray diffractometer with a nonmonochromated Cu K_α X-ray source. HT-XRD was a carried in H$_2$/Ar = 5/95 (volume ratio) using a Bruker D8 diffractometer equipped with an Mo $K_{\alpha1}$ source, a lynkeyes detector position sensitive detector (PSD), and an Anton Paar XRK900 Reactive Chamber. The sample was placed in a Macor glass-ceramic sample holder and the data were collected in the range 2θ = 4°–35° (total counting time = 30 min per scan), with a 0.02° step from room temperature to 450 °C. The same heating and cooling rate of 5 °C min^{-1} was used. For high resolution HT-XRD, the data were collected in the range 2θ = 10.8°–13.6° (total counting time = 2 min per scan), with a 0.02° step from room temperature to 450 °C with a heating rate of 5 °C min^{-1}. The measurement was carried out in fixed angle mode taking advantage of the 2θ angular window of 3° of the Lynxeyes PSD detector. This allows fast measurement of a few minutes as a function of temperature by focusing on a small angular domain. In our case, the angular domain 10.8°–13.6° have been chosen because it contains two characteristic peaks of Sb$_2$S$_3$ and Sb at 11.39° and 13.09°, respectively. SEM images and energy dispersive spectroscopy (EDS) were collected with a JEOL-7100F SEM/EDS microscope at an acceleration voltage of 20 kV. TEM and HRTEM images were recorded by using a JEM-2100F scanning transmission electron microscopy (STEM)/EDS microscope. Brurauer–Emmerr–Teller surface areas were measured using a Tristar II 3020 instrument by adsorption of nitrogen at 77 K. XPS was collected by using a VG Multi Lab 2000 instrument. TG/differential scanning calorimeter (DSC) was performed using a Netzsch STA 449C simultaneous thermal analyzer at a heating rate of 10 °C min^{-1} in air. Raman spectra were collected through a Renishaw inVia Raman microscope. A 633 or 532 nm He–Ne laser was focused on the samples for different test condition.

Electrochemical Measurements: The electrochemical properties were evaluated by assembly of 2016 coin cells in a glove box filled with pure argon. In lithium half cells, lithium metal was used as the counter electrode. 1 M LiPF$_6$ in ethylene carbon (EC)/dimethyl carbonate (DMC)/ethyl methyl carbonate (1:1:1 vol/vol/vol) was used as electrolyte. In sodium half cells, sodium metal was used as the counter electrode. 1 M solution of NaClO$_4$ in EC/DMC (1: 1 w/w) with 5% fluorinated ethylene carbonate was used as the electrolyte. A whatman glass fiber membrane (GF/D) was used as the separator. The working electrodes were produced from a slurry with a weight ratio of 70% Sb@N-C active material, 20% ketjen black, and 10% carboxyl methyl cellulose. The slurry was pasted on copper foil and dried in an oven for 12 h at 70 °C. The average mass loading of the active material was ≈1.2 mg cm^{-2}. Galvanostatic charge–discharge measurement was performed using a multichannel battery testing system (LAND CT2001A). Voltammetry (CV) curves were recorded with an electrochemical workstation at different scan rates (Autolab PGSTAT 302).

Supporting Information

Supporting Information is available from the Wiley Online Library or from the author.

Acknowledgements

Conflict of Interest

The authors declare no conflict of interest.

Keywords

[1] M. Armand, J. M. Tarascon, *Nature* **2008**, *451*, 652.
[2] L. Mai, X. Tian, X. Xu, L. Chang, L. Xu, *Chem. Rev.* **2014**, *114*, 11828.
[3] J. Qin, C. He, N. Zhao, Z. Wang, C. Shi, E. Z. Liu, J. Li, *ACS Nano* **2014**, *8*, 1728.
[4] K. S. Wook, S. D. Hwa, X. Ma, C. Gerbr, K. Kang, *Adv. Energy Mater.* **2012**, *2*, 710.
[5] C. M. Park, J. H. Kim, H. Kim, H. J. Sohn, *Chem. Soc. Rev.* **2010**, *39*, 3115.
[6] M. Lao, Y. Zhang, W. Luo, Q. Yan, W. Sun, S. X. Dou, *Adv. Mater.* **2017**, *29*, 1700622.
[7] C. K. Chan, H. Peng, G. Liu, K. McIlwrath, X. F. Zhang, R. A. Huggins, Y. Cui, *Nat. Nanotechnol.* **2008**, *3*, 187.
[8] W. Luo, J. J. Gaumet, L. Mai, *Rare Met.* **2017**, *36*, 321.
[9] B. Farbod, K. Cui, W. P. Kalisvaart, M. Kupsta, B. Zahiri, A. Kohandehghan, E. M. Lotfabad, Z. Li, E. J. Luber, D. Mitlin, *ACS Nano* **2014**, *8*, 4415.
[10] A. Nie, L. Y. Gan, Y. Cheng, X. Tao, Y. Yuan, S. Sharifi-Asl, K. He, H. Asayesh-Ardakani, V. Vasiraju, J. Lu, F. Mashayek, R. Klie, S. Vaddiraju, U. Schwingenschlögl, R. Shahbazian-Yassar, *Adv. Funct. Mater.* **2016**, *4*, 543.
[11] M. D. Slater, D. Kim, E. Lee, C. S. Johnson, *Adv. Funct. Mater.* **2013**, *23*, 947.
[12] H. Lv, S. Qiu, G. Lu, Y. Fu, X. Li, C. Hu, J. Liu, *Electrochim. Acta* **2015**, *151*, 214.
[13] A. Darwiche, C. Marino, M. T. Sougrati, B. Fraisse, L. Stievano, L. Monconduit, *J. Am. Chem. Soc.* **2012**, *134*, 20805.
[14] L. Baggetto, P. Ganesh, C. N. Sun, R. A. Meisner, T. A. Zawodzinski, G. M. Veith, *J. Mater. Chem. A* **2013**, *1*, 7985.
[15] W. Luo, P. Zhang, X. Wang, Q. Li, Y. Dong, J. Hua, L. Zhou, L. Mai, *J. Power Sources* **2016**, *304*, 340.
[16] W. Zhang, Y. Liu, C. Chen, L. Zhen, Y. Huang, X. Hu, *Small* **2015**, *11*, 3822.
[17] L. Liang, Y. Xu, C. Wang, L. Wen, Y. Fang, Y. Mi, M. Zhou, H. Zhao, Y. Lei, *Energy Environ. Sci.* **2015**, *8*, 2954.
[18] H. Kim, J. Cho, *Chem. Mater.* **2008**, *20*, 1679.
[19] H. Hou, M. Jing, Y. Yang, Y. Zhu, L. Fang, W. Song, C. Pan, X. Yang, X. Ji, *ACS Appl. Mater. Interfaces* **2014**, *6*, 16189.
[20] J. Liu, L. Yu, C. Wu, Y. Wen, K. Yin, F. K. Chiang, R. Hu, J. Liu, L. Sun, L. Gu, J. Maier, Y. Yu, M. Zhu, *Nano Lett.* **2017**, *17*, 2034.
[21] H. Hou, M. Jing, Y. Yang, Y. Zhang, Y. Zhu, W. Song, X. Yang, X. Ji, *J. Mater. Chem. A* **2015**, *3*, 2971.
[22] L. Wu, X. Hu, J. Qian, F. Pei, F. Wu, R. Mao, X. Ai, H. Yang, Y. Cao, *Energy Environ. Sci.* **2014**, *7*, 323.
[23] Y. Zhu, X. Han, Y. Xu, Y. Liu, S. Zheng, K. Xu, L. Hu, C. Wang, *ACS Nano* **2013**, *7*, 6378.
[24] N. Zhang, Y. Liu, Y. Lu, X. Han, F. Cheng, J. Chen, *Nano Res.* **2015**, *8*, 3384.
[25] X. Zhou, Y. Zhong, M. Yang, M. Hu, J. Wei, Z. Zhou, *Chem. Commun.* **2014**, *50*, 12888.
[26] X. Zhou, Z. Dai, J. Bao, Y. G. Guo, *J. Mater. Chem. A* **2013**, *1*, 13727.
[27] L. Hu, X. Zhu, Y. Du, Y. Li, X. Zhou, J. Bao, *Chem. Mater.* **2015**, *27*, 8138.
[28] Z. Liu, X. Y. Yu, X. W. Lou, U. Paik, *Energy Environ. Sci.* **2016**, *9*, 2314.
[29] N. Wang, Z. Bai, Y. Qian, J. Yang, *Adv. Mater.* **2016**, *28*, 4126.
[30] T. Ramireddy, M. Rahman M, T. Xing, Y. Chen, A. M. Glushenkov, *J. Mater. Chem. A* **2014**, *2*, 4282.
[31] Y. Yang, X. Yang, Y. Zhang, H. Hou, M. Jing, Y. Zhu, L. Fang, Q. Chen, X. Ji, *J. Power Sources* **2015**, *282*, 358.
[32] M. He, K. Kravchyk, M. Walter, M. V. Kovalenko, *Nano Lett.* **2014**, *14*, 1255.
[33] H. Hou, M. Jing, Y. Zhang, J. Chen, Z. Huang, X. Ji, *J. Mater. Chem. A* **2015**, *3*, 17549.
[34] H. Hou, M. Jing, Y. Yang, Y. Zhang, W. Song, X. Yang, J. Chen, Q. Chen, X. Ji, *J. Power Sources* **2015**, *284*, 227.
[35] L. Wu, H. Lu, L. Xiao, X. Ai, H. Yang, Y. Cao, *J. Mater. Chem. A* **2015**, *3*, 5708.
[36] Y. N. Ko, Y. C. Kang, *Chem. Commun.* **2014**, *50*, 12322.
[37] J. Qian, Y. Chen, L. Wu, Y. Cao, X. Ai, H. Yang, *Chem. Commun.* **2012**, *48*, 7070.
[38] C. Nithya, S. Gopukumar, *J. Mater. Chem. A* **2014**, *2*, 10516.
[39] W. Shen, C. Wang, Q. Xu, H. Liu, Y. Wang, *Adv. Energy Mater.* **2015**, *5*, 1400982.
[40] J. Xu, M. Wang, N. P. Wickramaratne, M. Jaroniec, S. Dou, L. Dai, *Adv. Mater.* **2015**, *27*, 2042.
[41] L. Qie, W. M. Chen, Z. H. Wang, Q. G. Shao, X. Li, L. X. Yuan, X. L. Hu, W. X. Zhang, Y. H. Huang, *Adv. Mater.* **2012**, *24*, 2047.
[42] A. Magasinski, P. Dixon, B. Hertzberg, A. Kvit, J. Ayala, G. Yushin, *Nat. Mater.* **2010**, *9*, 353.
[43] W. Li, G Zheng, Y. Yang, Z. Seh, N. Liu, Y. Cui, *Proc. Natl. Acad. Sci. USA* **2013**, *110*, 7148.
[44] J. Lu, T. Wu, K. Amine, *Nat. Energy* **2017**, *2*, 17011.
[45] M. Oezaslan, F. Hasché, P. Strasser, *Chem. Mater.* **2011**, *23*, 2159.
[46] X. Xiong, G. Wang, Y. Lin, Y. Wang, X. Ou, F. Zheng, C. Yang, J. H. Wang, M. Liu, *ACS Nano* **2016**, *10*, 10953.
[47] K. Mcguire, N. D. Lowhorn, T. M. Tritt, A. M. Rao, *J. Appl. Phys.* **2002**, *92*, 2524.
[48] H. B. Wang, T. Maiyalagan, X. Wang, *ACS Catal.* **2012**, *2*, 781.
[49] A. L. M. Reddy, A. Srivastava, S. R. Gowda, H. Gullapalli, M. Dubey, P. M. Ajayan, *ACS Nano* **2010**, *4*, 6337.
[50] L. J. Fu, K. Tang, K. P. Song, P. A. Van Aken, Y. Yu, J. Maier, *Nanoscale* **2014**, *6*, 1384.
[51] X. Zhou, L. Yu, X. Y. Yu, X. W. Lou, *Adv. Energy Mater.* **2016**, *6*, 1601177.
[52] X. Wang, C. Niu, J. Meng, P. Hu, X. Xu, X. Wei, L. Zhou, K. Zhao, W. Luo, M. Yan, L. Mai, *Adv. Energy Mater.* **2015**, *5*, 1500716.